Astron. Astrophys. 265, 257–267 (1992)

ASTRONOMY AND ASTROPHYSICS

The formation of helioseismology lines

II. Modeling of alkali resonance lines with granulation

J.H.M.J. Bruls and R.J. Rutten

Sterrekundig Instituut, Postbus 80 000, NL-3508 TA Utrecht, The Netherlands

Received March 27, accepted July 1, 1992

Abstract. We model the NLTE formation of the solar Na I and K I resonance lines for an array of one-dimensional atmospheric models taken from a numerical simulation of the solar granulation by Nordlund & Stein. We discuss the nature of alkali-line sensitivity to granulation using hot and cool extremes from the simulation and we study the granular modulation of diagnostics such as line bisectors and helioseismological resonance-cell response. We also show that granular structuring produces apparent spatially-averaged line broadening of similar magnitude as the ad-hoc microturbulent and damping broadening invoked in traditional plane-parallel modeling.

Key words: line: formation – line: profile – Sun: atmosphere – Sun: granulation – Sun: photosphere

1. Introduction

In sequel to Bruls et al. (1992, henceforth Paper I), we study the K I and Na I resonance lines in the solar spectrum. These lines are frequently employed as diagnostics of the dynamical structure of the solar atmosphere and—through helioseismology—of the solar interior; an introductory review with references is given in Paper I. Paper I analysed NLTE (Non-Local Thermodynamic Equilibrium) phenomena in their formation for standard plane-parallel models of the solar atmosphere. This paper is concerned with more realistic modeling taking three-dimensional (3D) granulation into account.

Earlier inhomogeneous alkali line formation studies, nearly all by the Naples group, employed schematic representations of photospheric granulation (Nelson 1978) and waves to compute K I 769.9 nm line profiles assuming NLTE invariancy (Marmolino et al. 1984, 1987, 1988, Severino et al. 1986, Gomez et al. 1987, 1991, Bonet et al. 1991; cf. Caccin et al. 1991). In the mean time, numerical solar granulation modeling has advanced markedly (e.g. Nordlund 1982, Hurlburt et al. 1984, Chan & Sofia 1989, Stein & Nordlund 1989, Steffen et al. 1989, Nordlund & Stein 1990, 1991, Steffen 1991, Cattaneo et al. 1991; see also Rutten & Severino 1989 and Spruit et al. 1990), to sufficient realism to be employed in studying detailed effects of granulation on emergent line profiles (Nordlund 1984b, 1985c, 1991, Lites et al. 1989). In this paper, we improve on the Naples example by combining much more detailed NLTE computation with a much more detailed description of the solar granulation, taken from a recent Nordlund & Stein simulation. We employ the latter by computing emergent line profiles for a selection of its surface elements, in 1D fashion along vertical lines of sight neglecting lateral photon exchange. We so add another step along the (long) way from simplified 1D modeling to the very complex 3D radiation-hydrodynamics description which the actual solar atmosphere requires.

Send offprint requests to: J.H.M.J. Bruls

2. Method and models

As in Paper I, we use version 2.0 of the radiative transfer code MULTI (Carlsson 1986) with modifications to account for the "line haze" in the ultraviolet. The atomic models are shown in Figs. 1 and 2. They are the largest "confection" model atoms derived in Paper I and furnish excellent representations of the alkali population processes and their sensitivity to non-local radiation fields.

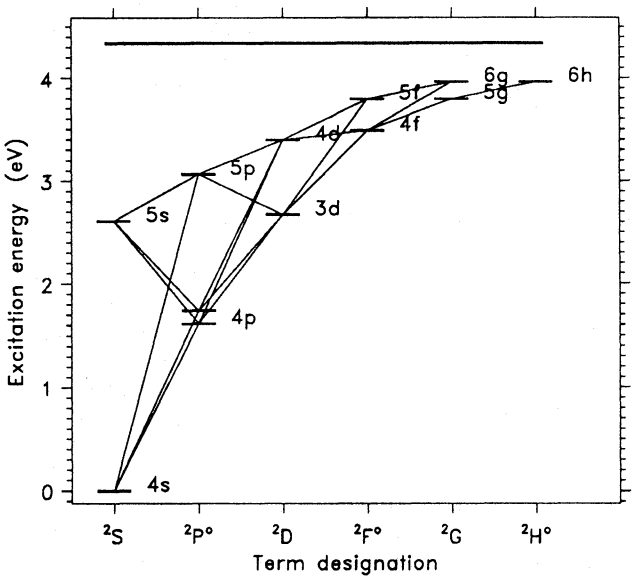

Fig. 1. Grotrian diagram of the K I model atom

We do not apply any microturbulence or damping enhancement factors. Sizable damping enhancements have been employed

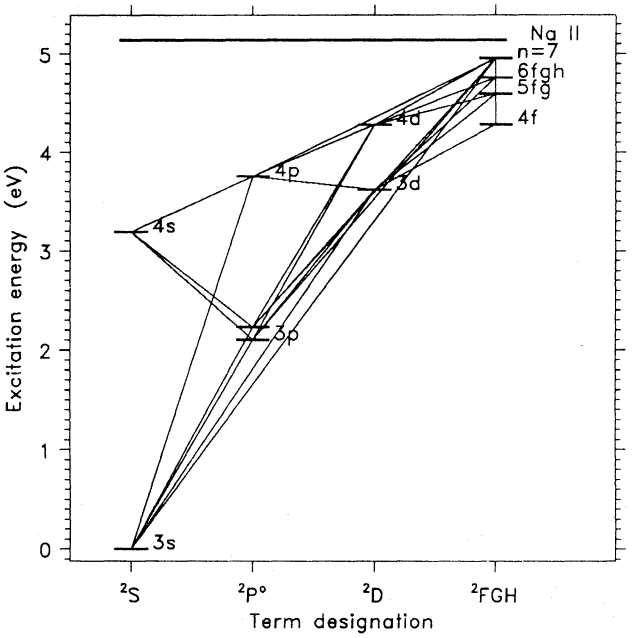

Fig. 2. Grotrian diagram of the Na I model atom. Vertical scaling equal to Fig. 1

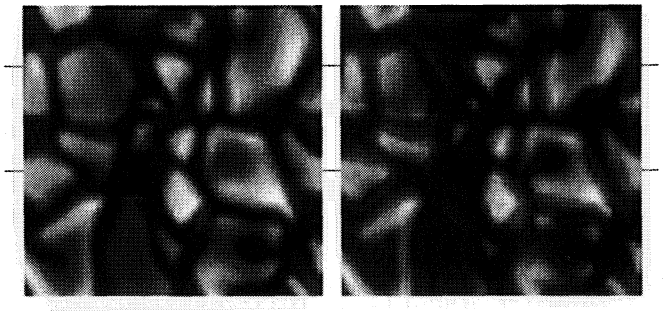

Fig. 3. Nordlund & Stein granulation simulation snapshot measuring 6000 × 6000 km. Left: emergent continuum intensity. Right: electron temperature at optical depth unity. The marks identify two slices chosen for the present analysis; we refer to the lower as slice 1, the upper as slice 2

in most plane-parallel modeling (e.g. Holweger 1971, Holweger & Müller 1974, Evans & Testerman 1975, Gurtovenko & Kondrashova 1980, Gomez et al. 1987a, Gomez et al. 1991) and are also obtained from comparison with alkali laboratory data (Andretta et al. 1991); nevertheless, we discard their usage as well as microturbulent broadening because Nordlund's (1984b) Fe I example suggests that observed excess line broadening over plane-parallel modeling may have more to do with atmospheric inhomogeneity than with true turbulence or atomic collision formalisms.

The input granulation simulation data consist of a "snapshot" cube of solar material for a single time step from one of the elastic time-dependent Nordlund & Stein computations (cf. Stein & Nordlund 1989, Nordlund & Stein 1990). It has a 63 × 63 horizontal grid and 47 depth points, constituting a cube of 6000 × 6000 × 1150 km^3. Figure 3 displays the emergent λ = 500 nm continuum intensity and the electron temperature T_e at continuum optical depth τ_{500} = 1. We limit our modeling

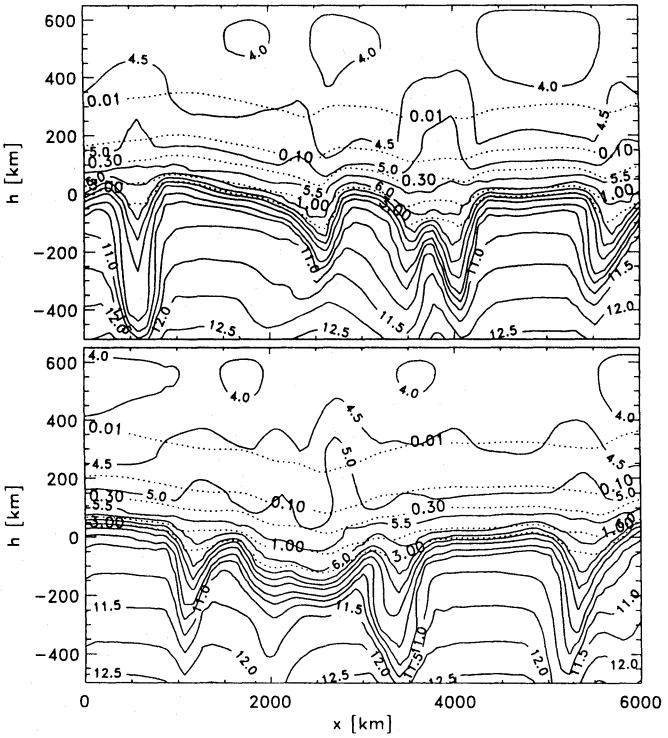

Fig. 4. Temperature in units of 10^3 K (solid; smaller contour annotation) and continuum optical depth (dotted; larger contour annotation) across simulation slices. Top: slice 2. Bottom: slice 1. Slices identified in Fig. 3

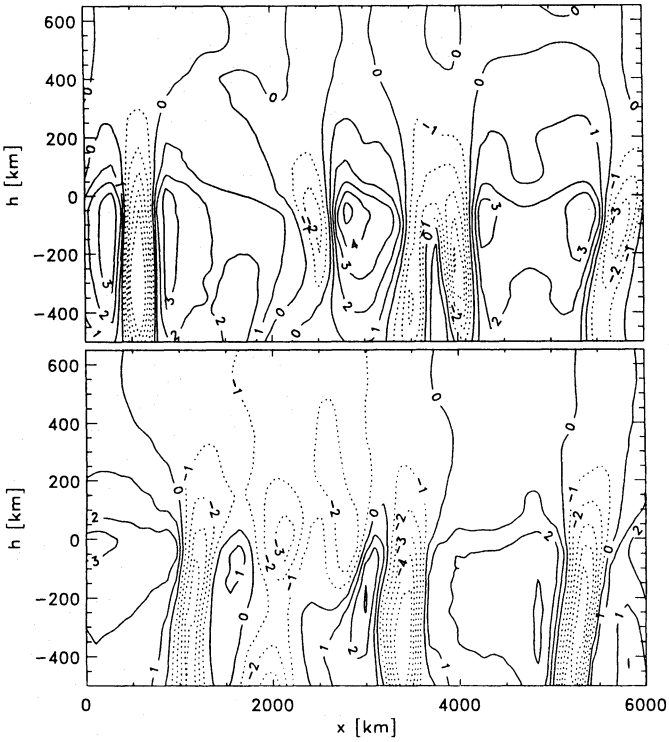

Fig. 5. Vertical velocity in km s^{-1} across simulation slices. Solid: upward motion. Dotted: downward motion. Top: slice 2. Bottom: slice 1. Slices identified in Fig. 3

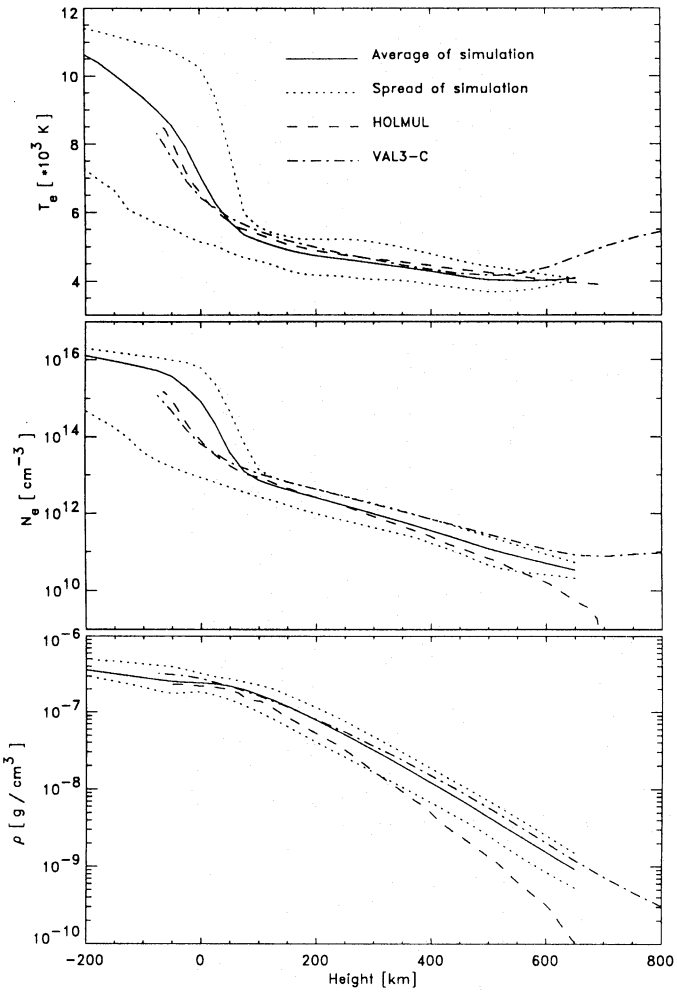

Fig. 6. State parameters against height. Top: electron temperature. Middle: logarithm of the electron density. Bottom: logarithm of the mass density. Dotted: upper and lower boundary of the variation per height point over all 126 stratifications in the two slices identified in Fig. 3. Solid: average over the 126 stratifications per height point. Dashed: HOLMUL standard model atmosphere. Dot-dashed: VAL3-C standard model atmosphere. The height scale of each stratification is defined by the original depth grid of the simulation and does not necessarily have $h = 0$ at $\tau_{500} = 1$. Each standard model is plotted on its own height scale, with $h = 0$ at $\tau_{500} = 1$

to the two slices of 63 columns each marked in Fig. 3, each column employed as a 1D model atmosphere. Figs. 4 and 5 display contour lines for the temperature, optical depth and vertical velocity variations along the two slices. They illustrate characteristic granulation patterns, large hot granules having wide and moderate upflows while the intergranular lanes are much narrower and cooler and contain fast downflows.

The simulation results are somewhat arbitrary in the highest layers, which require spectral line modeling in more detail than is currently achieved (e.g. Nordlund 1985b, 1991, Spruit et al. 1990, Steffen 1991). The simulation used here has a fiducial layer of 150 km thickness at the top (Nordlund & Stein 1990) to provide an open boundary zone for mass motions through the actual upper boundary at $h = 500$ km (Fig. 5). As a result, the same temperature is reached at $h = 650$ km for each horizontal grid point (Fig. 6). In addition, lines as strong as the Na I D lines are not optically thin at the top of the simulation cube. All 126 columnar stratifications have therefore been extended with the chromospheric part of the VAL3-C atmosphere (Vernazza et al. 1981, Fig. 6) by applying linear transitions in T_e and in the logarithms of the electron density N_e and hydrogen density N_H across a span of 150 km (about one scale height) centered at $h = 500$ km. Figure 6 shows that such simple transitions are appropriate. The vertical velocities are arbitrarily set to decay linearly to zero across the 150 km wide transition zone.

3. Results

3.1. Hot and cool examples

We have selected two extreme examples from the 126 stratifications, respectively representing a hot rising granule and a cool descending intergranular lane. The photospheric temperature drop of the hot model is steeper than for the VAL3-C quiet Sun model; the cool model is slightly less steep. Figures 7–11 show results.

The top panels of Fig. 7 show that the ground-level population departure coefficients $\beta = n/n^{\mathrm{LTE}}$ (defined following Wijbenga & Zwaan 1972) are smaller by a factor of 2–4 for the hot model than for the cool model above $h \approx 100$ km. The two model temperatures are nearly the same at this height; the divergence results from the ionizing ultraviolet radiation which is more superthermal ($J_\nu > B_\nu$) above the hot granule than above the cool intergranular lane. The NLTE photon suction process (see Paper I) produces an initial increase of the cool-model departure coefficients to $\beta > 1$ above $h \approx 100$ km. The subsequent downturn near $h = 350$ km and the rise above $h = 500$ km are due to the increasing domination of NLTE photoionization. For the hot model, photoionization dominates over photon suction at all heights so that β drops below unity already near $h = 100$ km for all levels. Thus, the factor 2–4 difference is due to effective photon suction in the cool model and effective overionization in the hot model.

The bound-bound photon pumps in the alkalis (4*s*–5*p* in K I, 3*s*–4*p* in Na I; see Paper I) are also more effective for the hot model, but their influence is only significant for higher levels than the ones involving the resonance lines. The 3*d* levels are an essential part of the recombination channel for both K I and Na I, both for direct recombination and for indirect recombination through photon suction replenishment along the Rydberg levels (Paper I). The deep dip of the 3*d* departure coefficients represents appreciable net recombination directly into 3*d*, but it does not inhibit photon suction which is driven independently by line photon losses.

The ground-level departure coefficients β_{4s} and β_{3s} affect the optical depth scalings shown in Fig. 8. Although the background continuum opacities are the same above $h = 575$ km for all stratifications, the hot-model line opacities lie below the cool-model opacities in this region due to the larger amount of NLTE overionization for the hot model. In deeper layers, the larger densities of the hot model win, producing larger line and continuum opacities.

The NLTE S^{L}/B_ν behavior of the resonance line source functions S^{L} (middle panels of Fig. 7) is set by the upper to lower level departure ratio $\beta_{\mathrm{u}}/\beta_{\mathrm{l}}$. These ratios are less sensitive to model differences than the coefficients themselves because β_{u} and β_{l} behave similarly. The ratios are displayed for slice 1 in Fig. 9. Their average behaviour is set by resonance-line photon

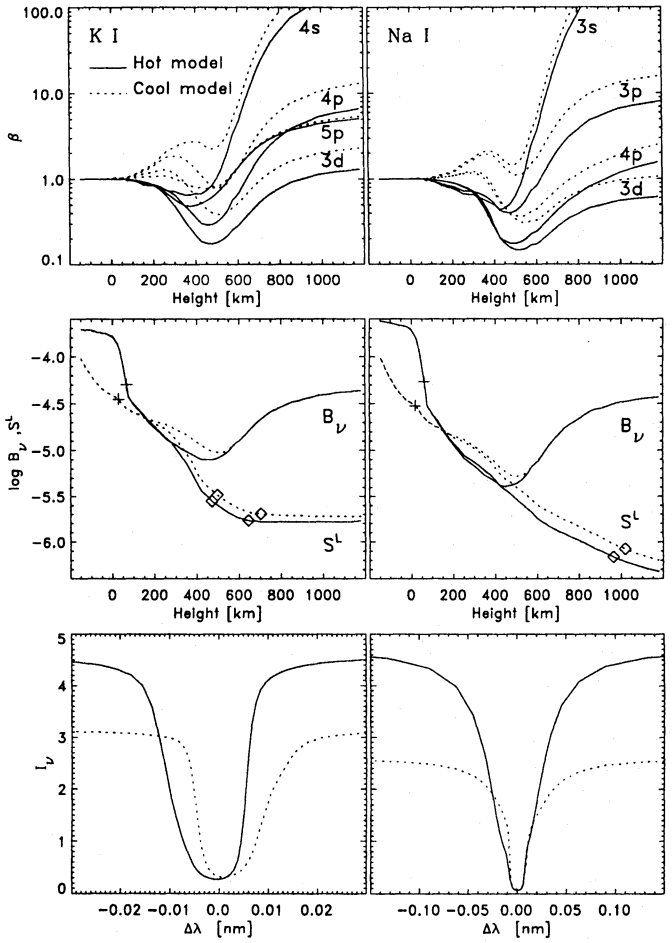

Fig. 7. K I (left) and Na I (right) results for representative hot (solid) and cool (dotted) granular models. Top panels: population departure coefficients $\beta = n/n^{\mathrm{LTE}}$. Only the four most relevant β's are plotted per element. Middle panels: resonance line source functions S^{L} and Planck functions $B_\nu(T_e)$. Pluses refer to optical depth $\tau_c = 1$ in the continuum near the line, diamonds to line-center optical depths $\tau_{\nu_0} = 1$ and $\tau_{\nu_0} = 0.1$ (the latter fall off-scale for Na I D_1). Bottom panels: computed profiles of K I 769.9 and Na I D_1. Note wavelength scale difference between K I and Na I panels. Units of B_ν, S_ν and I_ν: 10^{-5} erg cm^{-2} s^{-1} Hz^{-1} sr^{-1}

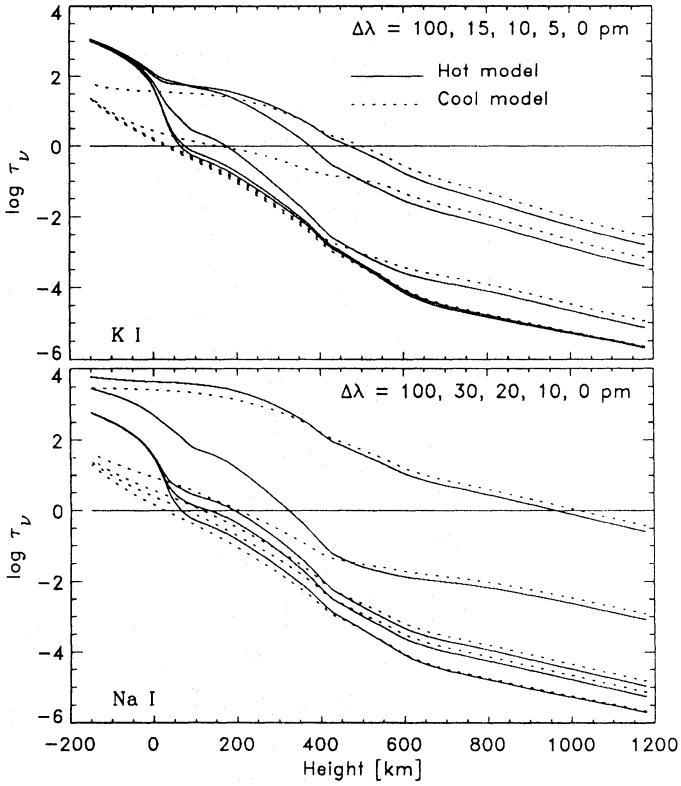

Fig. 8. Optical depth scaling of the K I (top) and Na I (bottom) resonance lines, for the hot model (left) and the cool model (right). The curves for K I specify τ_ν at $\Delta\lambda = 0$, 5, 10, 15 & 100 pm from line center (on the long-wavelength side; from top to bottom, respectively). Na I D_1 curves are for $\Delta\lambda = 0$, 10, 20, 30 and 100 pm from line center

losses (cf. Fig. 8 of Paper I); the rms variation from the mean is small. For example, at $h = 500$ km (which is near the $\tau_{\nu_0} = 1$ location for K I 769.9 nm, cf. Fig. 10) the rms variations of K I β_{4s} and β_{4p} are 35–40% from their mean, whereas the rms variation in their ratio β_{4p}/β_{4s} is only 7%.

The resulting resonance line profiles (bottom panels of Fig. 7) display the temperature and opacity differences between the two models mainly as difference in continuum intensity. The line center intensities are not very sensitive to the model differences because they originate above the steep temperature drop in the deep photosphere where the horizontal temperature variations are largest. The line center intensities actually display slight reversed contrast, due to the temperature cross-over between the hot and cool models which is evident as Planck function cross-over in the middle panels of Fig. 7.

The widths of the line wings are also not very different between the hot and the cool model since they are formed in similar conditions (near the pluses in the middle panels). However, the granular up- and downflows and velocity gradients produce their familiar pronounced signatures: blueshift and more extended blue wing for hot upflowing material, redshift and a deeper red wing for cool downflowing material. The redshifts exceed the blueshifts because the downflows have larger velocity than the upflows and also because the lines are formed deeper for the cool model, sampling yet larger velocities.

3.2. *Contribution functions*

Figures 10 and 11 display line depression contribution functions following Magain (1986). The lefthand ordinates are specified in velocity units to enable direct comparison between K I and Na I. The corresponding emergent profiles (thick curves) are the same as in Fig. 7, but normalized per model to the emergent continuum intensity. Note the pronounced velocity-induced asymmetry in the contribution functions between the blue and the red wings, the change in preferred wing between the hot and the cool model, and the double peaks present in some inner-wing contribution functions. The latter arise from the height variation of the Doppler width, which follows the temperature since we apply no microturbulent smearing; the widening with height caused by the chromospheric temperature rise adds extra line opacity above $h = 500$ km and produces a second maximum for the curves near the extinction-profile transition between damping wings and Doppler core. At the figure limits of $\Delta v = \pm 12$ km s^{-1} the wings have nearly reached the continuum for K I (Fig. 10), but only 40–70% of the continuum intensity for Na I (Fig. 11).

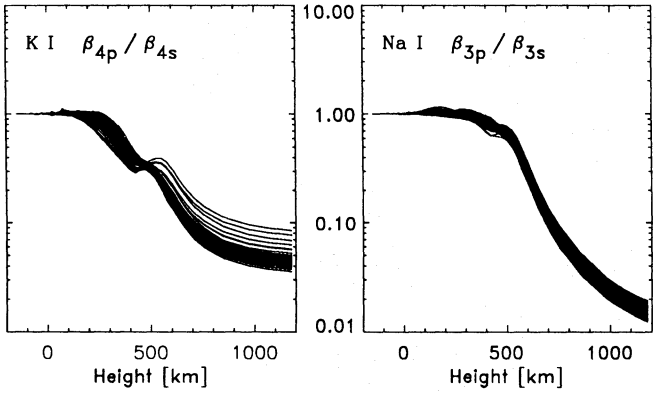

Fig. 9. K I and Na I resonance-line ratios of upper and lower departure coefficients, for all stratifications of slice 1. The ratio β_u/β_l sets the deviation of the line source function from the Planck function. It is less model-sensitive than the individual departure coefficients

3.3. Variation along slices

Figure 12 displays results computed from all 126 stratifications in the two slices. The top panels show line profiles per surface element of the first slice. The continuum variation is very large, due to the sizable temperature differences and steep gradients which occur at the height of continuum formation. The line-center intensity variation is much smaller due to the near-homogeneity of the temperature at line-center formation height.

Many profiles have inverted wing–core intensity contrast (darker wings and brighter cores than average) produced by the temperature cross-overs of the hotter and cooler stratifications near $h = 100$ km (Fig. 7; above this height, models termed "hot" are actually cooler than the ones called "cool"). Such negative correlations have been observed in other lines (e.g. Holweger & Kneer 1989). They are also evident in the intensity comparisons in Fig. 13, in which the line-center intensity curves (dotted) tend to be similar but reversed in sign to the intensity variations of the adjacent continua (solid). The continuum intensity shows larger modulation near Na I D_1 than near K I 769.9 nm because it forms deeper and has larger Planck function response to temperature variations; the morphology is the same, however.

The K I line core emerges much deeper than the Na I core (Figs. 10 and 11) but the two line cores display about the same inhomogeneity in relative intensity modulation, with remarkably similar patterns. The similarity illustrates that both line source functions are dominated by scattering of photons which originate in the photosphere near $h = 200$ km, only slightly above the cross-over locations and only slightly deeper for the K I core than for the Na I core.

The middle panels of Fig. 12 display the corresponding line bisectors. The excess of large redshifts illustrates that intergranular downflows tend to be faster than granular upflows. The convergence of the lower Na I bisectors results from our choice to let the vertical velocities decline to zero across the transition zone to the extension model. The distinct difference in upper-bisector shapes between K I and Na I portrays difference in line extinction. The K I resonance line does not extend much beyond its Doppler core, so that its opacity and formation height vary strongly with wavelength across the whole line. The Na I D lines, however, have wide damping wings extending from the Doppler core; these have much slower variation of opacity and formation

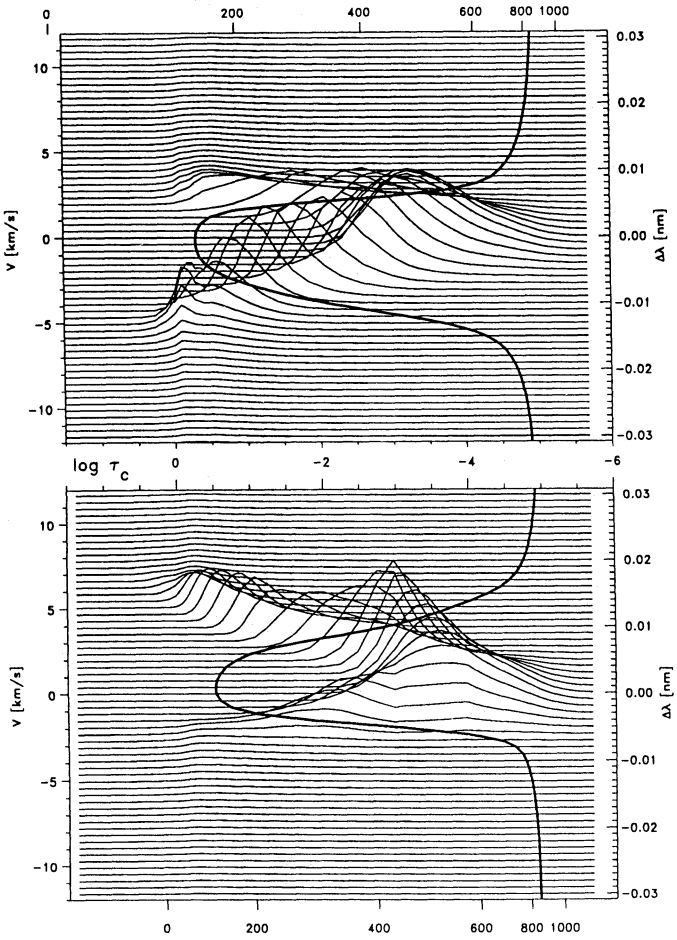

Fig. 10. K I 769.9 nm line depression contribution functions for the hot model (top) and the cool model (bottom). Abscissae: logarithm of local continuum optical depth, given between panels; corresponding heights in km are indicated at the top and bottom for the two models, respectively. Ordinates: wavelength separation from line center, measured in km s^{-1} (left) and nm (right). The flat part of each curve specifies its zero level and wavelength; the curves are area-normalized to the line depression at their wavelength. The thick solid curves are the corresponding emergent profiles, zero intensity corresponding to $\log \tau_c = 0$, continuum intensity to $\log \tau_c = -5$

height with wavelength. Consequently, the K I bisectors show variation throughout the profiles whereas the Na I D bisectors show variation only in the Doppler core, at low residual intensity. This difference is also seen in Figs. 10 and 11 in which only the Na I profiles reach the slowly-varying damping regime with noticeable line depression, producing broad ridges in Fig. 11 which barely shift in location.

The bottom panels of Fig. 12 display averaged line profiles and bisectors, shown separately for the two slices to illustrate that two such "spectrograph-slit" spatial averages may differ considerably. The differences between the two bisector averages seem rather large, but such large variation over the solar surface agrees with observations; Roca-Cortes et al. (1983) find considerable K I bisector changes even between larger surface areas. The panels also include observed spatially-averaged line profiles and their bisectors. These come from an unpublished digital absolute-intensity atlas of the disk-center solar spectrum

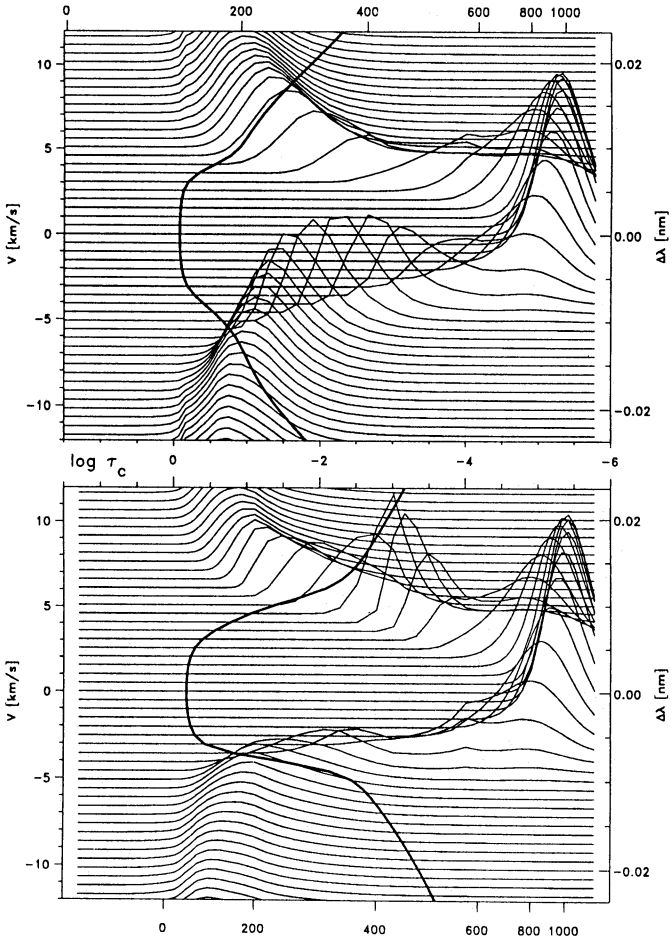

Fig. 11. Na I D_1 line depression contribution functions for the hot model (top) and the cool model (bottom). Coding as in Fig. 10. Note that the ordinate scaling (in km s^{-1}) is the same as for Fig. 10; for Na I D_1 its range covers only the inner part of the line

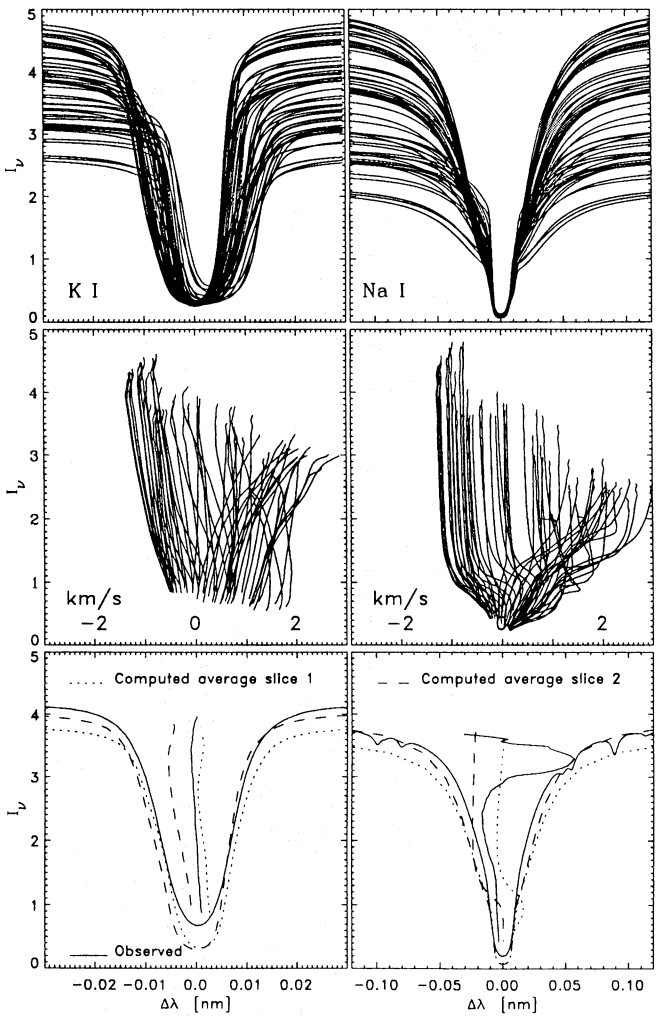

Fig. 12. Computed K I (left) and Na I D_1 (right) line profiles (top), bisectors (middle) and slice averages (bottom). The line profiles and line bisectors are for all 63 stratifications of slice 1, representing a 6000 km long slit projected on the solar surface. Averages for each of the two slices, of both profiles and bisectors, are shown separately in the bottom panels; spatially-averaged disk-center observed profiles and bisectors are added for comparison (solid). Bisectors are plotted on the velocity scale indicated in the middle panels, also the bisectors in the bottom panels. The upper observed Na I bisector is disturbed by blends. Ordinate units: 10^{-5} erg cm^{-2} s^{-1} Hz^{-1} sr^{-1}

prepared by H. Neckel from high-quality National Solar Observatory FTS data and calibrated with data of Neckel & Labs (1984)(cf. Rutten 1988).

Finally, Fig. 14 displays rms intensity variations across the resonance line profiles. The two sets of curves represent extreme choices for the upper-atmosphere velocity extrapolations, respectively vanishing and constant with height. The differences between the two sets are small. The continuum rms contrast ranges from 15% near the K I line to 22% near the Na I line, similar to the results of Nordlund (1984a). The line center contrast is much lower, reflecting the smaller temperature variations near $h = 200$ km where the line-center intensities are controlled. The peak-and-valley patterns across the line wings result primarily from Doppler shifts. The inner-wing peaks are lower for Na I due to higher formation. The dips in the blue wings again reflect temperature cross-overs above granules and intergranular lanes. The dip in the red Na I wing results from less pronounced damping wings in the intergranular profiles; there is no dip in the red K I wing because this line has almost no damping wings.

4. Discussion

4.1. Selection effects

The slices in Fig. 3 were selected to display representative granulation variations. However, the observed profiles in Fig. 12 come from area-averaged observations which may differ in statistics. Figure 15 shows continuum intensity distributions evaluated from Fig. 3. The top panel shows the distribution for the two slices, the bottom panel for the whole simulation surface. The slice distribution (top) has a slightly higher high-intensity tail than the distribution over the whole cube (bottom).

The lower panel of Fig. 15 also contains an observed continuum intensity distribution, determined from high-resolution filtergrams obtained with the SOUP tunable filtergraph of the Lockheed Palo Alto Research Laboratories and the Swedish vac-

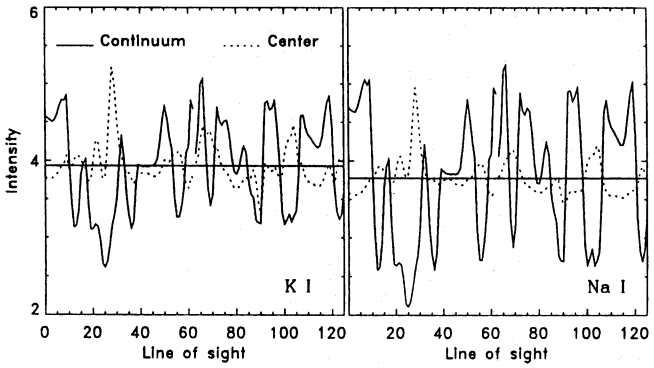

Fig. 13. Comparison between continuum (solid) and line center (dotted) intensity variations for all 126 models, for the K I resonance line (left) and Na I D_1 (right). The gap at center marks the slice transition. The line center intensities have been multiplied by 5 for K I and 20 for Na I while the mean values have been offset to coincide with the mean continuum intensity (horizontal lines). Ordinate units: 10^{-5} erg cm^{-2} s^{-1} Hz^{-1} sr^{-1}

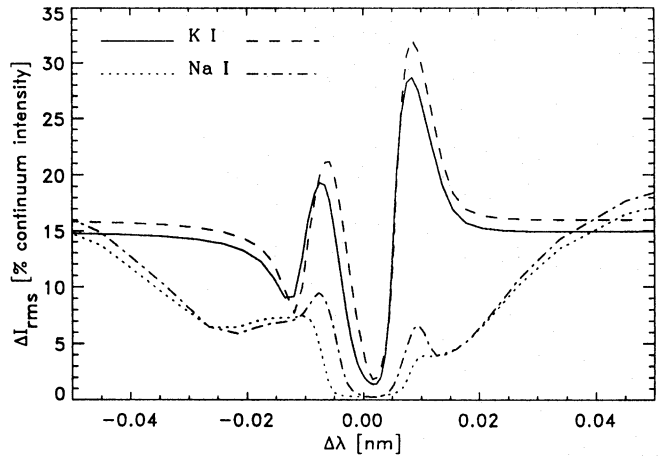

Fig. 14. Computed rms intensity contrast across K I and Na I resonance lines in percent of the mean continuum intensity. Solid and dotted curves are for standard extension with vanishing upper-atmosphere velocities. Other curves are for constant upward continuation of the velocities of the granulation simulation at $h = 575$ km

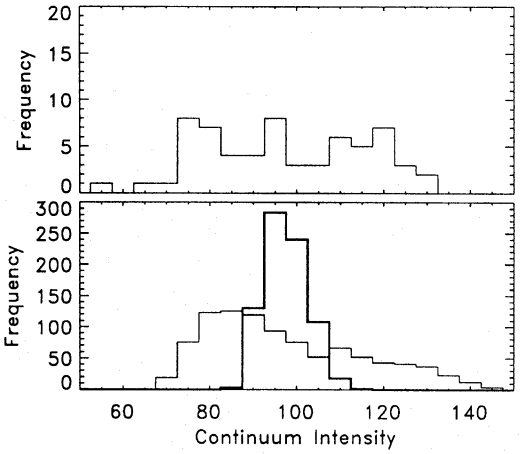

Fig. 15. Continuum intensity distributions. Bins are 5% of mean intensity; mean intensities set equal to 100. Top: distribution over both slices. Bottom: distribution over the whole simulation cube (thin), compared with observed distribution for a quiet-Sun region of comparable size (thick). The computed intensities were first averaged to the spatial resolution of the observations

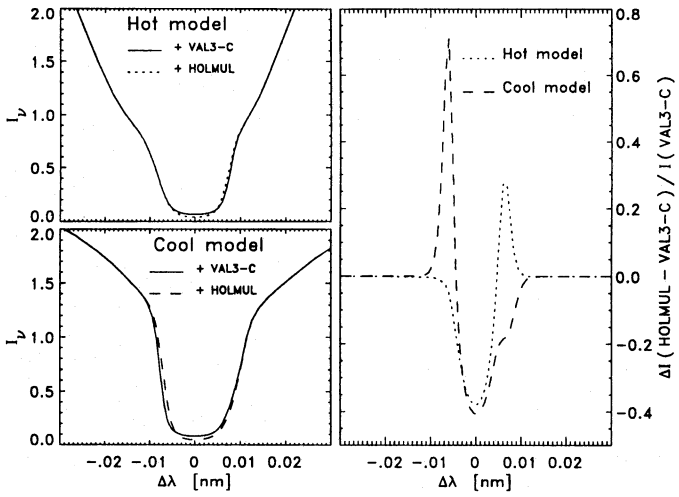

Fig. 16. Left: Na I D_1 line core profile for representative hot and cool models with VAL3-C (solid) and HOLMUL (dashed) extensions; ordinate units: 10^{-5} erg cm^{-2} s^{-1} Hz^{-1} sr^{-1}. Right: relative line profile difference between the two model extensions

uum solar telescope on La Palma. The computed distribution is much wider than the observed one, which is not surprising since the simulation continuum contrast (Fig. 14) is also larger than typical observed rms contrasts. This difference may well be due to insufficient spatial resolution and image degradation by atmospheric seeing in the observations (cf. Nordlund 1984a, 1985a). The computed continuum intensity distribution also deviates from the observed distribution in being asymmetric, favoring the lower intensities. Nordlund & Stein (1991) attribute this asymmetry to temperature–velocity correlation; its absence in the observed distribution suggests that the narrower intergranular lanes were not fully resolved.

4.2. Upper-atmosphere extensions

The cores of the Na I D lines are sensitive to the extensions of the simulation data with the VAL3-C quiet-Sun model. The Na I D source functions are dominated by scattering and set already in the lower photosphere, but the observed line-center Dopplershift is imparted in the chromospheric layers where the line-depression contribution function peaks. The K I line, including its Doppler signal, is formed below the extension height.

The influence of the extensions is tested in Fig. 16 by comparing the standard VAL3-C extensions for the hot and cool stratifications with similar extensions employing the HOLMUL chromosphere-less LTE atmosphere (Holweger & Müller 1974, see Fig. 6). The differences are very small. The relative intensity differences (HOLMUL − VAL3-C)/VAL3-C (righthand panel) have peaks at the edge of the Doppler core due to small differential wavelength shifts. They are caused by the smaller line opacities for the HOLMUL model, larger escape depths sampling larger granulation velocities. The line-center differences are set by the line source functions. S^L is smaller for the HOLMUL extension because its upper-atmosphere temperature and

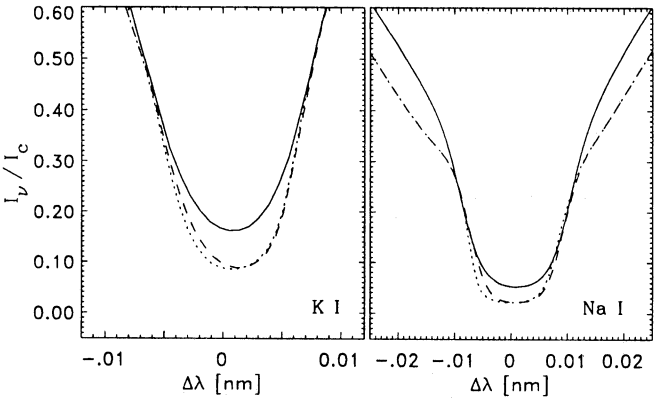

Fig. 17. Spatially-averaged line core profiles of K I 769.9 nm (left) and Na I D_1 (right), each normalized to the continuum intensity. Solid: observation. Dotted: vanishing granular velocities in upper atmosphere. Dashed: non-vanishing granular velocities in upper atmosphere

corresponding B_ν are lower, whereas the ratio S^L/B_ν is set by scattering and is nearly model-independent.

Our choice to let the granular flows vanish across the transition layer to the extension model is directly reflected by the convergence of the lower Na I D bisectors in the middle-right panel of Fig. 12. We test the effect on the emergent intensity in Fig. 17. The other extreme, outward continuation of all simulation velocities at $h = 575$ km, produces only minor differences.

4.3. Comparison with observations

The computed average line and continuum intensities in Fig. 12 are slightly lower than the observed values. The continuum differences are surprisingly small, considering that the simulation employs only four frequencies to represent the whole spectrum and that the simulation opacities differ from ours. Figure 18 shows the same computed and observed profiles but rescaled to the background continua. This normalization largely eliminates effects from opacity differences and indeed improves the agreement.

The computed line cores are wider and more boxy than the observed ones. Figure 17 shows that this difference is not due to our choice to let the granular motions vanish in the upper atmosphere. It may result from our neglect of solar oscillations. Figure 18 shows that "macroturbulent" velocity broadening of order 2 km s^{-1} (corresponding to rms velocity of 1.4 km s^{-1}) brings the K I line core in good agreement with the observed profile.

The Na I D core is fitted less well; 3 km s^{-1} broadening produces about the correct line-center intensity but not the observed boxy shape (inset). Note that 3 km s^{-1} conforms to the nonthermal broadening of the VAL3-C model at $h \approx 1000$ km where the Na I D_1 core emerges (Fig. 11; Fig. 11 of Vernazza et al. 1981); this value may be taken as upper limit to the line-broadening effect of wave motions. Thus, it seems unlikely that the boxy shape of the Na I D_1 core is caused by oscillations alone, or by other purely velocity-related effects for which Gaussian smearing would be a valid description. The next paper of this series shows that the alkali cores are also not sensitive to effects of partial frequency redistribution. We speculate that the nonlinear wave phenomena apparent in the formation of the so-called Ca II H_{2V} and K_{2V} cell grains (reviewed by Rutten & Uitenbroek 1991) contribute to the formation of the Na I D_1 core as well. Computation of

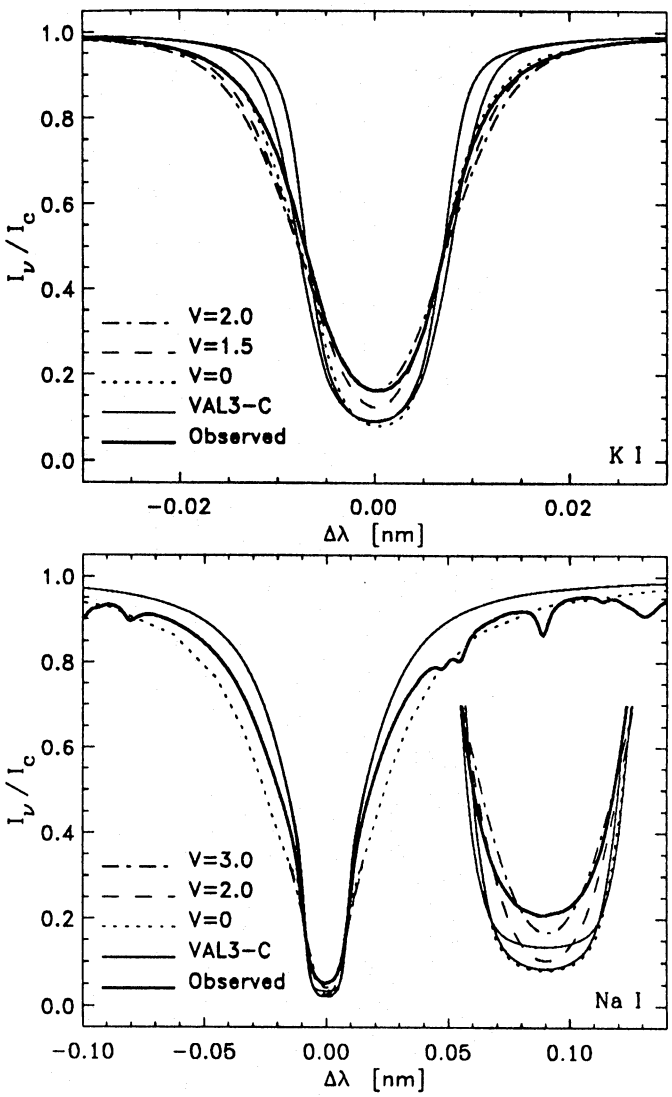

Fig. 18. Spatially-averaged line profiles of K I 769.9 nm (top) and Na I D_1 (bottom). Computed profiles are averaged over all 126 models and normalized to the continuum intensity, then smeared with the specified macroturbulence V. Only the $V = 0$ curve is shown in the Na I D_1 wings where the three curves coincide. Thin solid curves: plane-parallel VAL3-C line profiles with and without microturbulent broadening. Thick solid curves: observed spatially-averaged profiles. Inset: Na I D_1 line cores on 4× expanded scales (both wavelength and intensity)

the Na I D lines within the detailed hydrodynamical simulations of chromospheric shocks by Rammacher & Ulmschneider (1992) and Carlsson & Stein (1992) would be worthwhile.

The computed K I line wings agree well with the observed profile, but the inner wings of the averaged Na I D_1 profiles are wider than the observed profile by approximately 3 km s^{-1} in both directions. The line wings are only slightly sensitive even to the largest velocity smearing in Fig. 18 for the K I line, not at all for the Na I D_1 line. Furthermore, the oscillation velocities in the lower photosphere are only of order 0.35 km s^{-1} (Canfield 1976, Durrant et al. 1979). The Na I wing difference seems therefore too large to be caused by photospheric oscillations alone. The difference is also not due to selection effects since the two slice averages in Fig. 12 have about the same inner Na I wings. We sus-

pect that it may be due to our neglect of lateral photon exchange, to which the Na I wings are most sensitive since wing photons travel further than line-center photons while the photosphere is effectively thick in the Na I wings. Nordlund (1991) argues that line-to-continuum coupling through velocity gradients along the line of sight produces intensity enhancements; similar effects are likely to occur for lateral velocity gradients.

4.4. Comparison with plane-parallel modeling

Figure 18 also contains line profiles computed with our model atoms in traditional plane-parallel fashion. We used the VAL3-C model atmosphere and two different choices of microturbulence, respectively $v = 0\,\mathrm{km\ s^{-1}}$ and the VAL3-C depth-dependent values which vary from $v = 0.6\,\mathrm{km\ s^{-1}}$ at the temperature minimum to $2.4\,\mathrm{km\ s^{-1}}$ at $h = 1000\,\mathrm{km}$. Van der Waals damping was again applied without enhancement factor. The resulting profiles (thin curves) are too deep, have too boxy cores and have too narrow wings compared with the observed profiles, both for K I 769.9 nm and for the Na I D_1 line and for either choice of microturbulence. This comparison illustrates the apparent necessity to apply damping enhancement factors to reproduce observed line broadening when modeling spatially-averaged profiles with a plane-parallel atmosphere.

In contrast, the spatially-averaged profiles computed from the Nordlund & Stein granulation simulation have too wide inner wings; their far wings fit the spatially-averaged observations well. The difference between the averaged Na I D_1 wings in Fig. 18 and the observed wings is of similar magnitude as the difference between the plane-parallel wings and the observed wings, but of opposite sign. This suggests that proper modeling of granular intensity modulation is a prerequisite before mismatch between profiles and spatially-averaged observations may be taken to imply failing line broadening formalisms, supporting Nordlund's (1984b) similar conclusion from profile fits of Fe I lines which originate from the same photospheric layers as the alkali line wings.

4.5. Alkali helioseismology

Sodium and potassium vapour cells are used in several programs to measure p-mode-induced photospheric velocities, either in scattering mode using full-disk irradiance or in two-cell transmission mode with spatial resolution (references in Paper I). The measuring principle concerning us here is the same for both types: scattered or transmitted intensities are alternatively measured using left and right circularly polarized Zeeman σ components as sampling windows which are magnetically displaced from the rest wavelength of the resonance line. The observed intensity ratio is linearly related to the Doppler shift of the line if both σ components sample a linear part of the line wings. However, if a σ component is too close to line center or to the continuum of a Doppler-shifted solar profile, the velocity determination cannot rely on a constant conversion factor. Additional measurement of $dI/d\lambda$ is sometimes achieved by slight variation of the magnetic field in the cell and used to improve the derived line shift. Intricate methods are devised to eliminate orbital and rotational offset velocities (Boumier et al. 1991, Pallé et al. 1992).

Let us give some examples. Gabriel et al. (1989) specify that the *Global Oscillations at Low Frequencies* (GOLF) instrument onboard the SOHO mission will measure Na I scattering in the σ components of both Na I D lines with intrinsic σ-component width of 2.5 pm and wavelength displacements of $\Delta\lambda = \pm 10$ pm

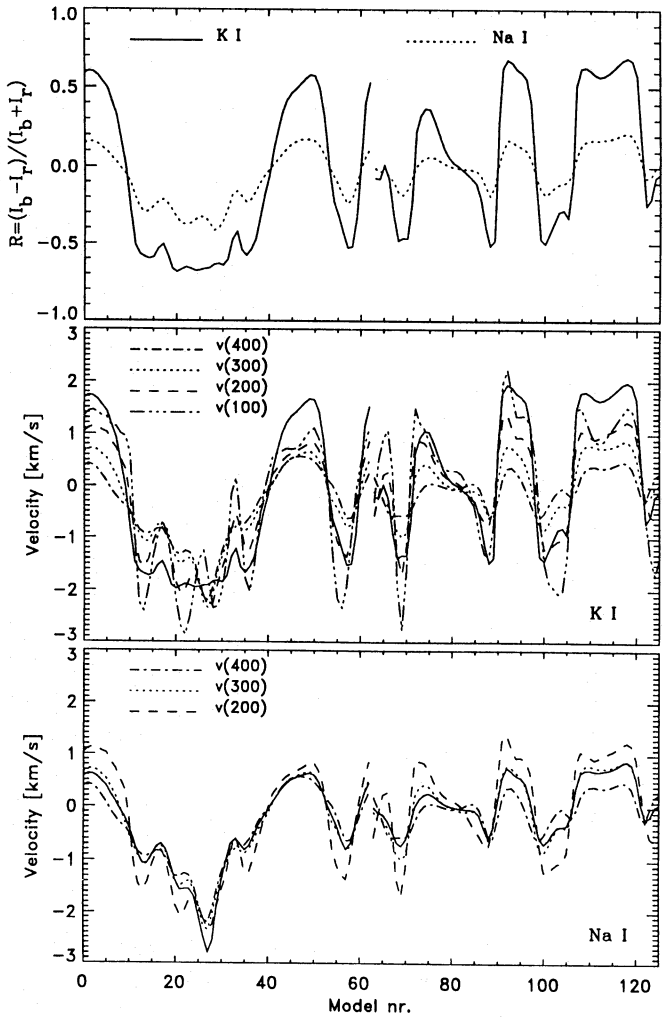

Fig. 19. Simulated helioseismology measurements. Top: K I and Na I D_1 line intensity ratios $R = (I_b - I_r)/(I_b + I_r)$ with I_b and I_r measured at the wavelength separations from line center used in helioseismology experiments, for all 126 stratifications in the two slices marked in Fig. 3. The gap in the middle marks the transition from the first slice to the second. Note the presence of large ratios for K I. Middle and bottom: corresponding line-of-sight velocities (solid) compared with the actual simulation velocities at three heights, coded as indicated. The K I velocities (middle panel) were derived from the intensity ratios in the top panel with the conversion factor proposed by Brookes et al. (1978) The Na I velocities (bottom panel) were derived from the intensity ratios in the top panel and local profile derivatives following Boumier et al. (1991) Boumier et al. (1991)

using a magnetic field of B =4750 Gauss. The velocity calibration employs magnetic field modulation. Potassium cells are used by the Birmingham–La Laguna group. Isaak et al. (1989) use a version described by Brookes et al. (1978) in which a 1800 Gauss magnetic field produces $\Delta\lambda = \pm 6.6$ pm σ-component displacements and from which the velocity is obtained by applying a constant multiplication factor to the observed intensity ratio. The transmission ("Cacciani") cells (e.g. Rhodes et al. 1988, Cacciani et al. 1990, 1991) exist in sodium and potassium versions and produce images in the σ-components transmitted through two tandem-mounted vapour cells. Velocities are similarly determined from intensity ratioing at a few wavelengths, producing

Dopplergrams (superimposed on orbital and rotational offsets); these have two-dimensional spatial resolution whereas the scattering cells measure full-disk averages only. The velocity signals in the latter are of course far smaller than the individual granular velocities which we model here.

The top panel of Fig. 19 displays σ-component intensity ratios from the emergent line profiles for all 126 stratifications in the two simulation slices. We used the σ-component displacements quoted above (respectively $\Delta\lambda = \pm 10$ pm for Na I and $\Delta\lambda = \pm 6.6$ pm for K I) and adopted a δ-function for the intrinsic σ-component absorption profile. This plot shows that for the K I 769.9 nm line, which is Doppler-shifted over 2.57 pm per km s^{-1} line-of-sight velocity, the measured intensity ratio exceeds the linear regime ($|R| \ll 0.5$) in many locations. The Na I intensity ratio behaves better, implying that Na I cells are capable of measuring larger velocities.

This expectation is born out by the middle and bottom panels, in which the solid curves show velocities derived from the intensity ratios in helioseismological manner. The contribution functions in Figs. 10 and 11 indicate that the resulting velocity signal should be representative of the actual velocities at heights $h = 200 - 400$ km for the specified σ-component displacements for both lines. The actual simulation velocities at four heights spanning $h = 100 - 400$ km are also plotted. Comparison shows that for Na I (bottom panel) the helioseismological estimate indeed follows the simulation velocities at $h = 300$ km very closely. For the K I line (middle panel) the esitmate fits none of the simulation curves closely, but it does follow their spatial patterns at larger amplitude, especially of the $h = 300$ km curve. A smaller conversion factor would improve the correspondence.

5. Conclusion

We have found that granulation simulations furnish a valuable testbed to study granulation-induced effects on solar spectral line formation. The present Nordlund & Stein simulation is probably not the final word in granulation modeling, but it does provide a range of parameters characteristic of what real solar line formation has to suffer from real solar granulation. Similarly, our neglect of lateral photon exchange represents a shortcoming to be remedied by future 3D radiative transfer modeling, but the variations displayed here for different surface elements at least indicate the error range of plane-parallel modeling.

For the alkali resonance lines, granulation-induced effects consist primarily of intensity variations set by the photospheric temperature stratification and of Doppler shifts imposed in the photosphere. These effects are sufficiently large that their inclusion reduces the need for ad-hoc microturbulent broadening and damping enhancement factors. The Doppler shifts measured by current K I and Na I resonance-cell seismometers register velocities at $h \approx 300$ km.

Acknowledgements. We are indebted to G. Severino and M.-T. Gomez for inspiration, to Å. Nordlund for supplying the Nordlund & Stein simulation data, to H. Neckel for supplying a copy of his FTS spectrum atlas, to L. H. Strous for measuring the intensity distribution of Fig. 15 and to C. J. Schrijver for suggesting that test.

References

Andretta, V., Gomez, M. T., Severino, G. 1991, Solar Phys., 131, 1
Bonet, J. A., Márquez, I., Vázquez, M., Wöhl, H. 1991, A&A, 244, 492
Boumier, P., Bocchia, R., Damé, L., Martic, M., Pallé, P., van der Raay, H. B., Robillot, J. M., Cortés, T. R. 1991, Adv. Space Res., 11,4, 199
Brookes, J. R., Isaak, G. R., van der Raay, H. B. 1978, MNRAS, 185, 1
Bruls, J. H. M. J., Rutten, R. J., Shchukina, N. G. 1992, A&A, in press (Paper I)
Cacciani, A., Smith, E., Zirin, H. 1991, in L. J. November (ed.), Solar Polarimetry, Proc. 11th NSO/SP Summer Workshop, National Solar Observatory, Sunspot, p. 133
Cacciani, A., Varsik, J., Zirin, H. 1990, Solar Phys., 125, 173
Caccin, B., Carlsson, M., Gomez, M. T., Severino, G. 1991, in L. Crivellari, I. Hubeny, D. G. Hummer (eds.), Stellar Atmospheres: Beyond Classical Models, NATO ASI Series C-341, KLuwer, Dordrecht, p. 415
Canfield, R. C. 1976, Solar Phys., 50, 239
Carlsson, M. 1986, A Computer Program for Solving Multi-Level Non-LTE Radiative Transfer Problems in Moving or Static Atmospheres, Report No. 33, Uppsala Astronomical Observatory
Carlsson, M., Stein, R. F. 1992, in M. Giampapa, J. M. Bookbinder (eds.), Cool Stars, Stellar Systems and the Sun, Proc. Seventh Cambridge Workshop, Astron. Soc. Pac. Conf. Series, in press
Cattaneo, F., Brummell, N. H., Toomre, J., Malagoli, A., Hurlburt, N. A. 1991, ApJ, 370, 282
Chan, K. L., Sofia, S. 1989, ApJ, 336, 1022
Durrant, C. J., Mattig, W., Nesis, A., Reiss, G., Schmidt, W. 1979, Solar Phys., 61, 251
Evans, J. C., Testerman, L. 1975, Solar Phys., 45, 41
Gabriel, A. H., Bocchia, R., Bonnet, R. M., Cesarsky, C., Christensen-Dalsgaard, J., Damé, L., Delache, P., Deubner, F.-L., Foing, B., Fossat, E., Fröhlich, C., Gorisse, M., Gough, D., Grec, G., Hoyng, P., Pallé, P., Paul, J., Robillot, J.-P., Roca Cortes, T., Stenflo, J. O., Ulrich, R. K., van der Raay, H. B. 1989, in The SOHO Mission – Scientific and Technical Aspects of the Instruments, ESA SP-1104, Paris, p. 13
Gomez, M. T., Marmolino, C., Roberti, G., Severino, G. 1987, A&A, 188, 169
Gomez, M. T., Rutten, R. J., Severino, G. 1991, A&A, 244, 501
Gurtovenko, E. A., Kondrashova, N. N. 1980, Solar Phys., 68, 17
Holweger, H. 1971, A&A, 10, 128
Holweger, H., Kneer, F. 1989, in R. J. Rutten, G. Severino (eds.), Solar and Stellar Granulation, NATO ASI Series C-263, Kluwer, Dordrecht, p. 173
Holweger, H., Müller, E. A. 1974, Solar Phys., 39, 19
Hurlburt, N. E., Toomre, J., Massaguer, J. M. 1984, ApJ, 282, 557
Isaak, G. R., McLeod, C. P., Pallé, P. L., van der Raay, H. B., Roca-Cortés, T. 1989, A&A, 208, 297
Lites, B. W., Nordlund, Å., Scharmer, G. B. 1989, in R. J. Rutten, G. Severino (eds.), Solar and Stellar Granulation, NATO ASI Series C-263, Kluwer, Dordrecht, p. 349
Magain, P. 1986, A&A, 163, 135
Marmolino, C., Roberti, G., Severino, G. 1987, Solar Phys., 108, 21
Marmolino, C., Roberti, G., Severino, G. 1988, in R. Viotti, A. Vittone, M. Friedjung (eds.), Physics of formation of FeII lines

outside LTE, Proc. IAU Coll. 94 (Capri), Reidel, Dordrecht, p. 217
Marmolino, C., Roberti, G., Vazquez, M., Severino, G., Wöhl, H. 1984, in E. Rolfe (ed.), Hydromagnetics of the Sun, Proc. Fourth European Meeting on Solar Physics, Noordwijkerhout, The Netherlands, ESA-SP220, p. 191
Neckel, H., Labs, D. 1984, Solar Phys., 90, 205
Nelson, G. D. 1978, Solar Phys., 60, 5
Nordlund, Å. 1982, A&A, 107, 1
Nordlund, Å. 1984a, in S. L. Keil (ed.), Small-Scale Dynamical Processes in Quiet Stellar Atmospheres, National Solar Observatory Summer Conference, Sacramento Peak Observatory, Sunspot, p. 174
Nordlund, Å. 1984b, in S. L. Keil (ed.), Small-Scale Dynamical Processes in Quiet Stellar Atmospheres, National Solar Observatory Summer Conference, Sacramento Peak Observatory, Sunspot, p. 181
Nordlund, Å. 1985a, Solar Phys., 100, 209
Nordlund, Å. 1985b, in H. U. Schmidt (ed.), Theoretical Problems in High Resolution Solar Physics, MPA/LPARL Workshop, Max-Planck-Institut für Physik und Astrophysik MPA 212, München, p. 1
Nordlund, Å. 1985c, in J. E. Beckman, L. Crivellari (eds.), Progress in stellar spectral line formation theory, NATO ASI Series C152, Reidel, Dordrecht, p. 215
Nordlund, Å. 1991, in L. Crivellari, I. Hubeny, D. G. Hummer (eds.), Stellar Atmospheres: Beyond Classical Models, NATO ASI Series C-341, KLuwer, Dordrecht, p. 61
Nordlund, Å., Stein, R. F. 1990, Comp. Phys. Comm., 59, 119
Nordlund, Å., Stein, R. F. 1991, in L. Crivellari, I. Hubeny, D. G. Hummer (eds.), Stellar Atmospheres: Beyond Classical Models, NATO ASI Series C-341, KLuwer, Dordrecht, p. 263
Pallé, P. L., Régulo, C., Corte'és, T. R., Duarte, L. S., Schmider, F. X. 1992, A&A, 254, 348
Rammacher, W., Ulmschneider, P. 1992, A&A, 253, 586
Rhodes, E. J., Cacciani, A., Garneau, G., Misch, T., Progovac, D., Shieber, T., Tomczyk, S., Ulrich, R. K. 1988, in R. C. Canfield, B. R. Dennis (eds.), MAX'91 Workshop #1, Summary and Reports, p. 33
Roca-Cortes, T., Vazquez, M., Wöhl, H. 1983, Solar Phys., 88, 1
Rutten, R. J. 1988, in G. Cayrel de Strobel, M. Spite (eds.), The Impact of Very High S/N Spectroscopy on Stellar Physics, IAU Symposium 132, Reidel, Dordrecht, p. 367
Rutten, R. J., Severino, G. (eds.) 1989, Solar and Stellar Granulation, NATO ASI Series C-263, Kluwer, Dordrecht
Rutten, R. J., Uitenbroek, H. 1991, Solar Phys., 134, 15
Severino, G., Roberti, G., Marmolino, C., Gomez, M. T. 1986, Solar Phys., 104, 259
Spruit, H. C., Nordlund, Å., Title, A. M. 1990, ARA&A, 28, 263
Steffen, M. 1991, in L. Crivellari, I. Hubeny, D. G. Hummer (eds.), Stellar Atmospheres: Beyond Classical Models, NATO ASI Series C-341, KLuwer, Dordrecht, p. 247
Steffen, M., Ludwig, H.-G., Krüß, A. 1989, A&A, 213, 371
Stein, R. F., Nordlund, Å. 1989, ApJ, 342, L95
Vernazza, J. E., Avrett, E. H., Loeser, R. 1981, ApJS, 45, 635
Wijbenga, J. W., Zwaan, C. 1972, Solar Phys., 23, 265

This article was processed by the author using Springer-Verlag LaTeX A&A style file 1990.